Axisymmetric semi-analytical finite elements for modelling waves in buried/submerged fluid-filled waveguides

Michał K. Kalkowski*, Jennifer M. Muggleton, Emiliano Rustighi

Institute of Sound and Vibration Research, University of Southampton, Highfield, Southampton SO17 1BJ, UK

Abstract

Efficient and accurate predictions of wave propagation are a vital component of wave-based non-destructive interrogation techniques. Although a variety of models are available in the literature, most of them are suited to a particular wave type or a specific frequency regime. In this paper we present a multi-wave model for wave propagation in axisymmetric fluid-filled waveguides either buried or submerged in a fluid based on the semi-analytical finite elements. The cross-section is discretised with higher-order spectral elements to achieve high efficiency and the singularities resulting from adopting a Lobatto scheme at the axis of symmetry are handled appropriately. The surrounding medium is modelled with a perfectly matched layer, for which we derive optimal parameters only from the material properties and the geometry of the waveguide. To represent the fluid and the solid-fluid coupling, acoustic and structural-acoustic SAFE elements are formulated. We analyse both free waves and the forced response and validate the model against numerical results from the literature and experiments. All verifications show very good agreement. The implementation of the method in Python is made also available with this publication.

Keywords: wave propagation, waves in pipes, fluid-filled pipes, waves in embedded pipes, semi-analytical finite element, perfectly matched layer, spectral

*Corresponding author
Email address: M.Kalkowski@soton.ac.uk (Michał K. Kalkowski)

elements

1. Introduction

Acoustic waves propagating in buried or immersed pipes are perhaps the most common principle upon which modern non-destructive interrogation methods are developed [1, 2]. Both wavespeed and attenuation depend on the properties of the pipe, its contents and the surrounding medium and can be used to identify these properties or evaluate their change in time. Moreover, when incident upon a discontinuity, either in the pipe or in the surrounding medium, the waves scatter allowing for detection of defects or a weakened support. Finally, waves radiating from the pipe can be sensed at a ground surface and provide a basis upon which both the location and the condition of the pipe can be assessed. An essential ingredient for all these techniques is a reliable model for wave propagation in buried/submerged pipes with fluid. Although there is a considerable number of publications dealing with either waves in fluid-filled pipes or with waves in embedded cylinders, relatively few works tackle the complete problem that includes both the pipe, the fluid and the surrounding medium.

For obvious historical reasons, analytical approaches have been developed first. Dispersion curves and energy distributions for fluid-filled thin cylinders have been presented by Fuller and Fahy [3]. Pinnington and Briscoe derived low frequency approximations for both fluid-dominated and axial waves in free pipes. The effect of the surrounding fluid was investigated by e.g. Greenspon [4] and Sihna et al. [5]. The case of a solid medium restraining the pipe has been studied to some extent by Toki and Hakada [6] (in an earthquake engineering context) and by Jette and Parker [7].

The pipe, the surrounding medium and the contained fluid altogether were considered probably for the first time by Muggleton et al. [8–10] where both fluid-dominated and axial waves were studied based on a simplified interaction between the pipe and the soil/water. Subsequent refinements and extensions of that model allowing for inclusion of the shear coupling with lubricated contact [11], compact

contact [12] and evaluating torsional waves [13] were also published.

Despite the negligible computational cost and an immediate insight into the physics gained from closed-form expressions offered by the aforementioned models, they are often limited to a particular wave type and the low frequency range. A more versatile approach based on the global matrix method [14] was developed in the ultrasonic community and was successfully applied to the problem of embedded, fluid-filled cylinders [15, 16], among others. The global matrix method originates from the description of the motion of the structure as a superposition of bulk waves propagating in each layer (the number of layers and materials can be arbitrary). The fundamental formulation is analytical, but requires a numerical solution in the form of root-tracing which often offers a fast and accurate solution. However, for complex structures, root-tracing may become both inefficient and unreliable (as it strongly depends on the initial guess). Moreover, developing a universal tracing algorithm applicable to all configurations is a rather cumbersome task.

The limitations of analytical models can be circumvented with numerical methods which solve the dispersion equation as an eigenvalue problem, such as the semi-analytical finite element (SAFE) method. The fundamental concept behind SAFE is that the cross-section is discretised using finite elements and spatially harmonic motion is assumed in the direction of propagation [17, 18]. The governing equation is written as an eigenvalue problem which can easily be solved using any numerical package available. SAFE provides a stable and reliable solution at a cost of the finite element discretisation. However, the number of degrees of freedom is usually small for closed waveguides.

Modelling open (embedded) waveguides with SAFE raises several new challenges, of which the greatest is an efficient representation of the surrounding medium. Castaigns and Lowe [19] proposed the idea of an absorbing layer with material damping smoothly increasing away from the core. Their approach could be conveniently implemented in a commercial finite element package, but the size of the problem grew large for low wavespeed soils. Jia et al. [20] developed infinite elements that can be coupled to standard, solid SAFE elements and analysed the effect of soil on waves in hollow cylinders. Mazzotti et al. developed a hybrid approach

based on SAFE and 2.5D boundary element method [21–23]. This idea yielded very promising results and was validated with experiments. However, coupling of two quite complex methods poses additional challenges for implementation.

An alternative is to use perfectly matched layers (PML) to represent the embedding medium. PMLs are known for decades and have been successfully applied to a number of applications, particularly in the electromagnetic community [24]. Including PMLs in numerical models for elastic waves is a relatively new idea. Treyssède et al. [25] developed a SAFE-PML formulation for plate like structures with a cubic polynomial chosen as a stretching function. Soon after, Nguyen et al. [26] presented an analogous formulation applied to three-dimensional embedded waveguides. It was shown that for an acoustically slow surrounding medium, the size of the problem can grow large owing to the required number of elements per wavelength. As a remedy, Treyssède [27] applied spectral elements utilising higher-order polynomials to enhance the efficiency of the solution. Also recently, Duan et al. [28] developed an axisymmetric SAFE-PML formulation and proposed the use of an exponential stretching function, particularly well suited to wave problems.

A scaled boundary finite element method (SBFEM) is a good alternative to SAFE and has recently been applied to the problem of axisymmetric [29] and embedded waveguides [30–32]. SBFEM is a well-established numerical framework, particularly in earthquake engineering. For guided wave problems it has many similarities with SAFE, however, both the discretisation principle and solution procedure are different. In the references mentioned above, the authors simplified the problem by representing the surrounding medium with a dashpot boundary condition. Although their approach is simple and elegant, it cannot provide accurate results when the contrast between acoustic impedances is low.

Despite the impressive developments in the field of modelling of elastic waves in recent decades, to the best of authors' knowledge, no numerical model for waves in fluid-filled embedded/submerged pipes has been published. Therefore, in this paper we propose an axisymmetric SAFE formulation for embedded/submerged pipes with fluid. Both the pipe and the surrounding medium can be composed of a number of layers of different, generally anisotropic materials. We use higher-order

spectral elements (SEs), as they are better suited to wave propagation problems than standard finite elements. The singularities arising from the axisymmetric assumption applied to SEs are accounted for appropriately. The surrounding medium, which can be either solid or fluid, is represented by a perfectly matched layer. Thus, several different elements need to be derived for such problem, namely acoustic, structural-acoustic coupling, structural, and perfectly matched layer elements. Both the free wave solution and forced response are discussed and the formulation is validated against published numerical results and experimental measurements. The implementation of the proposed method in Python is also made available with this publication (details in the Acknowledgements section).

2. Derivation of SAFE elements

We consider an axisymmetric, infinitely long and uniform waveguide, where r and θ are the cross-sectional coordinates and z is the direction of propagation. The waveguide can be composed of any number of layers, either solid of fluid. Owing to the axisymmetric assumption the cross-section is represented with mono-dimensional elements. The most typical representation of such class of problems is an embedded/submerged fluid-filled pipe. The pipe scenario together with chosen labelling and conventions is shown in Fig. 1. SAFE formulations for all respective elements are presented in the following subsections.

2.1. Structural element

The structural (elastic) SAFE element is derived in a similar way to [18] but with slightly different conventions. We start from recalling the virtual work principle for deformable elastic bodies [33] which states that

$$\int_V \delta\bar{\mathbf{u}}^\top \rho \ddot{\bar{\mathbf{u}}}\, \mathrm{d}V + \int_V \delta\bar{\boldsymbol{\epsilon}}^\top \bar{\boldsymbol{\sigma}}\, \mathrm{d}V = \int_V \delta\bar{\mathbf{u}}^\top \bar{\mathbf{t}}\, \mathrm{d}V \tag{1}$$

where V is the volume occupied by the waveguide, $\bar{\mathbf{u}}$ is the displacement vector, ρ is the mass density, $\bar{\boldsymbol{\epsilon}}$ is the strain vector, $\bar{\boldsymbol{\sigma}}$ is the stress matrix, $\bar{\mathbf{t}}$ is the external traction and $\ddot{(\cdot)}$ symbol denotes double differentiation with respect to time. Our

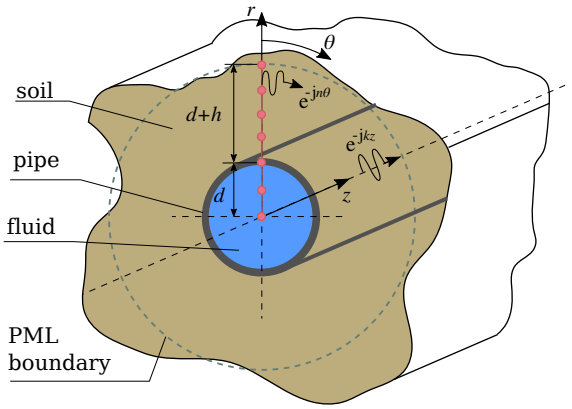

Figure 1: Schematic diagram outlining the problem and chosen coordinate conventions.

attention is focused on free wave propagation here, hence the right-hand side, i.e. the external traction is set to zero.

The displacement and strain vectors are defined as

$$\begin{aligned} \bar{\mathbf{u}} &= \begin{bmatrix} \bar{u}_r & \bar{u}_\theta & \bar{u}_z \end{bmatrix}^\top \\ \bar{\boldsymbol{\epsilon}} &= \begin{bmatrix} \bar{\epsilon}_{rr} & \bar{\epsilon}_{\theta\theta} & \bar{\epsilon}_{zz} & \bar{\gamma}_{\theta z} & \bar{\gamma}_{zr} & \bar{\gamma}_{r\theta} \end{bmatrix}^\top \end{aligned} \tag{2}$$

where γ are the engineering shear strains. The stress is related to the strain via the Hooke's Law:

$$\bar{\boldsymbol{\sigma}} = \mathbf{C}\bar{\boldsymbol{\epsilon}} \tag{3}$$

with $\mathbf{C}$ being the elasticity matrix.

The axial symmetry is represented by the harmonic variation of the displacement along the circumference. The variation of the displacement along θ is expressed as a Fourier series

$$\bar{\mathbf{u}}(r,\theta,z) = \sum_0^\infty \bar{\mathbf{u}}_n(u,z)\mathrm{e}^{-\jmath n\theta} \tag{4}$$

where n is an integer to ensure 2π-periodicity. For clarity, this assumption is not applied till the end of the derivation.

The strain is related to the displacement via differential operators:

$$\bar{\boldsymbol{\epsilon}} = \left(\frac{1}{r}\mathbf{L} + \mathbf{L}_r\frac{\partial}{\partial r} + \mathbf{L}_\theta\frac{1}{r}\frac{\partial}{\partial\theta} + \mathbf{L}_z\frac{\partial}{\partial z}\right)\bar{\mathbf{u}} \tag{5}$$

where the respective operators are:

$$\mathbf{L}=\begin{bmatrix}0&0&0\\1&0&0\\0&0&0\\0&0&0\\0&0&0\\0&-1&0\end{bmatrix},\quad \mathbf{L}_r=\begin{bmatrix}1&0&0\\0&0&0\\0&0&0\\0&0&0\\0&0&1\\0&1&0\end{bmatrix},\quad \mathbf{L}_\theta=\begin{bmatrix}0&0&0\\0&1&0\\0&0&0\\0&0&1\\0&0&0\\1&0&0\end{bmatrix},\quad \mathbf{L}_z=\begin{bmatrix}0&0&0\\0&0&0\\0&0&1\\0&1&0\\1&0&0\\0&0&0\end{bmatrix} \tag{6}$$

As in standard finite element procedures, the displacement within the element is approximated using shape functions, such that

$$\bar{\mathbf{u}}(r,\theta,z,t)=\mathbf{N}(r)\bar{\mathbf{q}}(\theta,z,t) \tag{7}$$

where $\bar{\mathbf{q}}(\theta,z,t)$ is a vector of nodal displacements. We can now rewrite Eq. (5) as

$$\bar{\boldsymbol{\epsilon}}=\left(\frac{1}{r}\mathbf{L}\mathbf{N}+\mathbf{L}_r\mathbf{N}_{,r}+\frac{1}{r}\mathbf{L}_\theta\mathbf{N}\frac{\partial}{\partial\theta}+\mathbf{L}_z\mathbf{N}\frac{\partial}{\partial z}\right)\bar{\mathbf{q}}=\mathbf{B}_1\bar{\mathbf{q}}+\mathbf{B}_2\frac{\partial}{\partial\theta}\bar{\mathbf{q}}+\mathbf{B}_3\frac{\partial}{\partial z}\bar{\mathbf{q}} \tag{8}$$

where $\mathbf{N}_{,r}$ denotes a derivative with respect to r and the $\mathbf{B}$ matrices are clearly defined in the last step.

Substituting Eq. (3) and Eq. (8) into Eq. (30) and assuming time harmonic motion, i.e. $\bar{\mathbf{q}}=\mathbf{q}e^{j\omega t}$, one obtains

$$\begin{aligned}&-\omega^2\int_V\delta\mathbf{q}^\top\mathbf{N}^\top\rho\mathbf{N}\mathbf{q}\,\mathrm{d}V+\\&\qquad\int_V\left(\delta\mathbf{q}^\top\mathbf{B}_1^\top+\frac{\partial}{\partial\theta}\delta\mathbf{q}^\top\mathbf{B}_2^\top+\frac{\partial}{\partial z}\delta\mathbf{q}^\top\mathbf{B}_3^\top\right)\mathbf{C}\left(\mathbf{B}_1\mathbf{q}+\mathbf{B}_2\frac{\partial}{\partial\theta}\mathbf{q}+\mathbf{B}_3\frac{\partial}{\partial z}\mathbf{q}\right)\mathrm{d}V=0\end{aligned} \tag{9}$$

where we note that in the cylindrical coordinates $\mathrm{d}V=r\,\mathrm{d}r\,\mathrm{d}\theta\mathrm{d}z$. The second integral in Eq. (9) needs to be integrated by parts, with terms involving derivatives over θ and over z being treated separately. After performing those integrations, the virtual work equation can now be written as

$$\begin{aligned}&\int_L\int_\theta\delta\mathbf{q}^\top\left(-\omega^2\mathbf{M}+\mathbf{K}_1\mathbf{q}-\mathbf{K}_2\mathbf{q}_{,\theta}-\mathbf{K}_3\mathbf{q}_{,z}-\mathbf{K}_4\mathbf{q}_{,z\theta}-\mathbf{K}_5\mathbf{q}_{,\theta\theta}-\mathbf{K}_6\mathbf{q}_{,zz}\right)\mathrm{d}\theta\,\mathrm{d}z+\\&\int_\theta\delta\mathbf{q}^\top\left(\mathbf{K}_{f1}^\top\mathbf{q}+\mathbf{K}_{f3}^\top\mathbf{q}_{,\theta}+\mathbf{K}_6\mathbf{q}_{,z}\right)\mathrm{d}\theta+\int_L\delta\mathbf{q}^\top\left(\mathbf{K}_{f1}+\mathbf{K}_5\mathbf{q}_{,\theta}+\mathbf{K}_{f3}\mathbf{q}_{,z}\right)\mathrm{d}z=0\end{aligned} \tag{10}$$

where for convenience we used subscript notation to denote differentiation and the matrices have been integrated over the cross-section (from r_0 to r_1) as denoted in the following

$$\begin{aligned}
\mathbf{K}_1 &= 2\pi \int_{r_0}^{r_1} \mathbf{B}_1^\top \mathbf{C}\mathbf{B}_1 r \,\mathrm{d}r & \mathbf{K}_{f1} &= 2\pi \int_{r_0}^{r_1} \mathbf{B}_1^\top \mathbf{C}\mathbf{B}_3 r \,\mathrm{d}r \\
\mathbf{K}_{f2} &= 2\pi \int_{r_0}^{r_1} \mathbf{B}_1^\top \mathbf{C}\mathbf{B}_2 r \,\mathrm{d}r & \mathbf{K}_{f3} &= 2\pi \int_{r_0}^{r_1} \mathbf{B}_2^\top \mathbf{C}\mathbf{B}_3 r \,\mathrm{d}r \\
\mathbf{K}_2 &= \mathbf{K}_{f2}^\top - \mathbf{K}_{f2} & \mathbf{K}_3 &= \mathbf{K}_{f1}^\top - \mathbf{K}_{f1} \\
\mathbf{K}_4 &= \mathbf{K}_{f3}^\top + \mathbf{K}_{f3} & \mathbf{K}_5 &= 2\pi \int_{r_0}^{r_1} \mathbf{B}_2^\top \mathbf{C}\mathbf{B}_2 r \,\mathrm{d}r \\
\mathbf{K}_6 &= 2\pi \int_{r_0}^{r_1} \mathbf{B}_3^\top \mathbf{C}\mathbf{B}_3 r \,\mathrm{d}r & \mathbf{M} &= 2\pi\rho \int_{r_0}^{r_1} \mathbf{N}^\top \mathbf{N} r \,\mathrm{d}r
\end{aligned} \tag{11}$$

The above integrations are typically performed using some kind of a Gauss quadrature.

From Eq. (10) we can deduce the governing equation for wave propagation in along z

$$\mathbf{K}_1\mathbf{q} - \omega^2\mathbf{M} - \mathbf{K}_2\mathbf{q}_{,\theta} - \mathbf{K}_3\mathbf{q}_{,z} - \mathbf{K}_4\mathbf{q}_{,z\theta} - \mathbf{K}_5\mathbf{q}_{,\theta\theta} - \mathbf{K}_6\mathbf{q}_{,zz} = 0 \tag{12}$$

and the natural boundary condition (resultant forces over the cross-section) along z:

$$\mathbf{K}_{f1}^\top\mathbf{q} + \mathbf{K}_{f3}^\top\mathbf{q}_{,\theta} + \mathbf{K}_6\mathbf{q}_{,z} = \mathbf{f}^z \qquad \text{or} \qquad \mathbf{q} = 0 \tag{13}$$

We now impose the n-periodicity of the displacement along the circumference as indicated in Eq. (4) and assume a spatially harmonic variation of the displacement along z, i.e. $\mathbf{q}_n(z) = \tilde{\mathbf{q}}_n \mathrm{e}^{-\jmath kz}$. Consequently, we arrive at the final form of the governing equation

$$\left(\mathbf{K}_1 - \omega^2\mathbf{M} + \jmath n\mathbf{K}_2 + \jmath k\mathbf{K}_3 + kn\mathbf{K}_4 + n^2\mathbf{K}_5 + k^2\mathbf{K}_6\right)\tilde{\mathbf{q}}_n = 0 \tag{14}$$

and the natural boundary condition

$$\left(\mathbf{K}_{f1}^\top - \jmath n\mathbf{K}_{f3}^\top - \jmath k\mathbf{K}_6\right)\tilde{\mathbf{q}}_n = \tilde{\mathbf{f}}^z \qquad \text{or} \qquad \tilde{\mathbf{q}}_n = 0 \tag{15}$$

2.2. Structure of the matrices

Matrices $\mathbf{K}_1$, $\mathbf{K}_4$, $\mathbf{K}_5$, $\mathbf{K}_6$ and $\mathbf{M}$ are symmetric, whereas matrices $\mathbf{K}_2$ and $\mathbf{K}_3$ are skew-symmetric ($\mathbf{K}_2 = -\mathbf{K}_2^\top$). The latter two matrices couple u_r with u_θ and u_r with u_z, respectively. The forms of u_θ and u_z are prescribed by the circumferential and axial periodicity, hence it is convenient to introduce a diagonal transformation matrix $\mathbf{T}$ as proposed in [34]. The transformation matrix has the same dimension as the SAFE matrices and each diagonal element corresponding to u_r is 1, whereas elements corresponding to u_θ and u_z are $\jmath$. Eq. (14) is premultiplied by $\mathbf{T}$ and $\tilde{\mathbf{q}}$ is replaced by $\mathbf{T}^*\mathbf{T}\tilde{\mathbf{q}}$, since $\mathbf{T}^*\mathbf{T} = \mathbf{I}$. Matrices $\mathbf{K}_1$, $\mathbf{K}_4$, $\mathbf{K}_5$, $\mathbf{K}_6$ and $\mathbf{M}$ remain unaltered by this operation, whereas $\mathbf{K}_2$ and $\mathbf{K}_3$ become

$$\begin{aligned} \mathbf{T}\mathbf{K}_2\mathbf{T}^* &= -\jmath\hat{\mathbf{K}}_2 \\ \mathbf{T}\mathbf{K}_3\mathbf{T}^* &= -\jmath\hat{\mathbf{K}}_3 \end{aligned} \tag{16}$$

where $\hat{\mathbf{K}}_2$ and $\hat{\mathbf{K}}_3$ are now symmetric. Eq. (14) can now be rewritten as

$$\left(\mathbf{K}_1 + n\hat{\mathbf{K}}_2 + n^2\mathbf{K}_5 - \omega^2\mathbf{M} + k\left(\hat{\mathbf{K}}_3 + n\mathbf{K}_4\right) + k^2\mathbf{K}_6\right)\mathbf{T}\tilde{\mathbf{q}} = 0 \tag{17}$$

2.3. Acoustic element

The acoustic SAFE element is derived below. We start from recalling the acoustic wave equation in terms of the velocity potential [35]

$$\nabla\cdot\nabla\phi - \frac{1}{c^2}\frac{\partial^2\phi}{\partial t^2} = 0 \tag{18}$$

In the above, ϕ is the velocity potential in the fluid and c is the speed of sound defined as

$$c = \sqrt{\frac{\beta}{\rho_f}} \tag{19}$$

with β being the bulk modulus and ρ_f – the mass density of the fluid. The velocity and pressure can be calculated from the potential as

$$\mathbf{v} = \nabla\phi \qquad\qquad p = -\rho\frac{\partial\phi}{\partial t} \tag{20}$$

The virtual work principle for fluids states that [33]

$$\int_{V_f}\delta\phi\,\frac{1}{c^2}\ddot{\phi}\,\mathrm{d}V + \int_{V_f}(\nabla\delta\phi)\cdot(\nabla\phi)\,\mathrm{d}V = 0 \tag{21}$$

where V_f is the volume occupied by the fluid. The velocity potential in the discretised medium is written as

$$\bar{\phi}(r,\theta,z,t) = \mathbf{N}_\phi(r)\boldsymbol{\phi}(z,\theta)\mathrm{e}^{J\omega t} \tag{22}$$

where $\mathbf{N}_\phi$ is the shape function matrix and $\boldsymbol{\phi}$ is the nodal velocity potential vector. In this paper, the shape functions for $\mathbf{N}_u$ and $\mathbf{N}_\phi$ are the same. The gradient operator is now also defined in the cylindrical coordinates

$$\nabla X = \begin{bmatrix} \frac{\partial X}{\partial r} & \frac{1}{r}\frac{\partial X}{\partial \theta} & \frac{\partial X}{\partial z} \end{bmatrix}^\top \tag{23}$$

so that

$$\nabla\phi = \nabla\left[\mathbf{N}_\phi(r)\boldsymbol{\phi}(\theta,z)\right] = \begin{bmatrix} \mathbf{N}_{\phi,r}\boldsymbol{\phi} & \frac{1}{r}\mathbf{N}_\phi\frac{\partial}{\partial\theta}\boldsymbol{\phi} & \mathbf{N}_\phi\frac{\partial}{\partial z}\boldsymbol{\phi} \end{bmatrix} \tag{24}$$

where the time-harmonic factor has been omitted for brevity.

Let us now substitute the finite element approximations into the virtual work equation

$$\begin{aligned} \frac{-\omega^2}{c^2}\int_{V_f}\delta\boldsymbol{\phi}^\top\mathbf{N}_\phi^\top\mathbf{N}_\phi\boldsymbol{\phi}\,\mathrm{d}V + \int_{V_f}\delta\boldsymbol{\phi}^\top\mathbf{N}_{\phi,r}^\top\mathbf{N}_{\phi,r}\boldsymbol{\phi}\,\mathrm{d}V \\ \int_{V_f}\delta\frac{\partial}{\partial\theta}\boldsymbol{\phi}^\top\frac{1}{r^2}\mathbf{N}_\phi^\top\mathbf{N}_\phi\frac{\partial}{\partial\theta}\boldsymbol{\phi}\,\mathrm{d}V + \\ \int_{V_f}\delta\frac{\partial}{\partial z}\boldsymbol{\phi}^\top\mathbf{N}_\phi^\top\mathbf{N}_\phi\frac{\partial}{\partial z}\boldsymbol{\phi}\,\mathrm{d}V = 0 \end{aligned} \tag{25}$$

After integrating the two last integrals by parts and noting that $\mathrm{d}V = r\,\mathrm{d}r\,\mathrm{d}\theta\mathrm{d}z$, we obtain

$$\begin{aligned} \int_L\int_\theta\delta\boldsymbol{\phi}^\top\left(-\omega^2\mathbf{M}\boldsymbol{\phi} + \mathbf{K}_1\boldsymbol{\phi} - \mathbf{K}_5\boldsymbol{\phi}_{,\theta\theta} - \mathbf{K}_6\boldsymbol{\phi}_{,zz}\right)\mathrm{d}\theta\,\mathrm{d}z + \\ \int_\theta\delta\boldsymbol{\phi}^\top\mathbf{K}_6\boldsymbol{\phi}_{,z}\,\mathrm{d}\theta + \int_L\delta\boldsymbol{\phi}^\top\mathbf{K}_5\boldsymbol{\phi}_{,\theta}\,\mathrm{d}z = 0 \end{aligned} \tag{26}$$

where the respective matrices are defined as follows (to maintain consistency, we kept the same subscript notation as for the structural element)

$$\begin{aligned} \mathbf{M} &= 2\pi\int_{r_0}^{r_1}\frac{1}{c^2}\mathbf{N}_\phi^\top\mathbf{N}_\phi r\,\mathrm{d}r & \mathbf{K}_1 &= 2\pi\int_{r_0}^{r_1}\mathbf{N}_{\phi,r}^\top\mathbf{N}_{\phi,r}r\,\mathrm{d}r \\ \mathbf{K}_5 &= 2\pi\int_{r_0}^{r_1}\frac{1}{r^2}\mathbf{N}_\phi^\top\mathbf{N}_\phi r\,\mathrm{d}r & \mathbf{K}_6 &= 2\pi\int_{r_0}^{r_1}\mathbf{N}_\phi^\top\mathbf{N}_\phi r\,\mathrm{d}r \end{aligned} \tag{27}$$

From Eq. (26) we can deduce the SAFE governing equation for wave propagation and the natural boundary condition (resultant pressure over the cross-section). Confining our attention to waves propagating along the z direction, we impose the circumferential periodicity condition and assume harmonic variation of the displacement along z, i.e. $\boldsymbol{\phi}_n(z) = \tilde{\boldsymbol{\phi}}_n \mathrm{e}^{-\jmath kz}$, to obtain

$$\left(\mathbf{K}_1 - \omega^2\mathbf{M} + n^2\mathbf{K}_5 + k^2\mathbf{K}_6\right)\tilde{\boldsymbol{\phi}}_n = \mathbf{0} \tag{28}$$

and

$$\tilde{\mathbf{p}} = (-\jmath k\mathbf{K}_6 - \jmath n\mathbf{K}_5)\,\tilde{\boldsymbol{\phi}}_n \tag{29}$$

For an acoustic problem, all matrices are symmetric and no transformation is required as in the case of structural elements. While applying the $\mathbf{T}$ transformation to the global matrices of the assembled coupled fluid-solid problem, respective entries at the diagonal of $\mathbf{T}$ corresponding to fluid velocity potential degrees of freedom are set to 1.

2.4. Coupling element

Finally, in this section we derive a structural-acoustic coupling relationships following the approach of Nilsson and Finnveden [36]. Let us start from stating the virtual work principle for both the structural and acoustic part, including the interaction forces. For the former we have (assuming no external traction)

$$\int_{V_s} \delta\bar{\mathbf{u}}^\top \rho_s \ddot{\bar{\mathbf{u}}}\,\mathrm{d}V + \int_{V_s} \delta\bar{\boldsymbol{\epsilon}}^\top \bar{\boldsymbol{\sigma}}\,\mathrm{d}V = \delta W_f \tag{30}$$

The virtual work done on the structure by the fluid pressure, W_f is represents the coupling between the two media

$$\delta W_f = \int_S \delta\mathbf{n}^\top \mathbf{u} p\,\mathrm{d}S \tag{31}$$

$\mathbf{n}$ is a vector normal to the wetted surface – in this case $\mathbf{n} = \begin{bmatrix} 1 & 0 & 0 \end{bmatrix}^\top$ and S is the wetted surface of contact between the structure and the fluid. In the above, the energy flow into the shell is defined positive [36]. Substituting the finite element approximations and noting that $p = -\rho\dot{\phi}$ one writes

$$\delta W_f = -\jmath\omega\rho \int_S \delta\mathbf{q}^\top \mathbf{N}_u^\top \mathbf{n}\mathbf{N}_\phi \boldsymbol{\phi}\,\mathrm{d}S = -\jmath\omega\rho\,\delta\mathbf{q}^\top \mathbf{H}\boldsymbol{\phi} \tag{32}$$

where $\mathbf{H} = \int_S \mathbf{N}_u^\top \mathbf{n} \mathbf{N}_\phi \, \mathrm{d}S$ is defined in the last step.

Likewise, the virtual work principle for the acoustic part is written as

$$\int_{V_f} \delta\phi \frac{1}{c^2} \ddot{\phi} \, \mathrm{d}V + \int_{V_f} (\nabla \delta\phi) \cdot (\nabla \phi) \, \mathrm{d}V = \delta W_s \tag{33}$$

Here, W_s is the virtual work done on the fluid by the structure. The latter is written as

$$\delta W_s = -\int_S \delta p \mathbf{n}^\top \mathbf{u} \, \mathrm{d}S \tag{34}$$

where the minus sign originates from the chosen convention for the direction of energy flow. Employing finite element approximations, one obtains

$$\delta W_s = \jmath \omega \rho \int_S \delta \boldsymbol{\phi}_i^\top \mathbf{N}_\phi^\top \mathbf{n}^\top \mathbf{N}_u \mathbf{q} \, \mathrm{d}S = \jmath \omega \rho \delta \boldsymbol{\phi}_i^\top \mathbf{H}^\top \mathbf{q} \tag{35}$$

Eq. (32) and Eq. (35) are the coupling terms which are the only modifications to the governing equations for the structural and acoustic parts derived above. It is noted that since $\mathbf{H}$ couples $\boldsymbol{\phi}_r$ with $\mathbf{q}$, it will interact with the $\mathbf{K}_1$ matrix only. Let us now write the governing equation for the assembly of structural and acoustic elements including the coupling term. The coupling terms need to be formulated appropriately to the application, i.e. whether it is supposed to represent fluid contained within a structure (e.g. pipe), or a fluid surrounding a structure. The equations below refer to the former case.

Under the axisymmetric assumption, the wetted surface is represented by one node. The surface integral becomes

$$\int_S (\cdot) \, \mathrm{d}S = \int_\theta (\cdot) r_s \, \mathrm{d}S = 2\pi r_s (\cdot) \tag{36}$$

where r_s is the coordinate of the fluid-structure interface. The integral in the coupling term can be simplified to

$$\mathbf{H} = 2\pi r_s \mathbf{N}_u(r_s)^\top \mathbf{n} \mathbf{N}_\phi(r_s) \tag{37}$$

The assembly of a fluid and structural elements including the coupling is now writ-

ten as

$$\left(-\omega^2 \begin{bmatrix} \tilde{\mathbf{M}} & \mathbf{0} \\ \mathbf{0} & \mathbf{M} \end{bmatrix} + \begin{bmatrix} \tilde{\mathbf{K}}_1 + n^2\tilde{\mathbf{K}}_5 & \mathbf{0} \\ \mathbf{0} & \mathbf{K}_1 + n\hat{\mathbf{K}}_2 + n^2\mathbf{K}_5 \end{bmatrix} + \jmath\omega \begin{bmatrix} \mathbf{0} & \rho\mathbf{H}^\top \\ -\rho\mathbf{H} & \mathbf{0} \end{bmatrix} + k \begin{bmatrix} \mathbf{0} & \mathbf{0} \\ \mathbf{0} & \hat{\mathbf{K}}_3 + n\mathbf{K}_4 \end{bmatrix} + k^2 \begin{bmatrix} \tilde{\mathbf{K}}_6 & \mathbf{0} \\ \mathbf{0} & \mathbf{K}_6 \end{bmatrix} \right) \begin{Bmatrix} \boldsymbol{\phi} \\ \mathbf{q} \end{Bmatrix} = \mathbf{0} \tag{38}$$

where the tilde symbols over the matrices denote that they correspond to the acoustic part of the structure. The symmetry is lost in the above problem, as the matrix with coupling terms is skew-symmetric. However, we can multiply the top row of the block matrix equation (corresponding to the fluid) by -1 to obtain

$$\left(-\omega^2 \begin{bmatrix} -\tilde{\mathbf{M}} & \mathbf{0} \\ \mathbf{0} & \mathbf{M} \end{bmatrix} + \begin{bmatrix} -\tilde{\mathbf{K}}_1 - n^2\tilde{\mathbf{K}}_5 & \mathbf{0} \\ \mathbf{0} & \mathbf{K}_1 + n\hat{\mathbf{K}}_2 + n^2\mathbf{K}_5 \end{bmatrix} + \jmath\omega \begin{bmatrix} \mathbf{0} & -\rho\mathbf{H}^\top \\ -\rho\mathbf{H} & \mathbf{0} \end{bmatrix} + k \begin{bmatrix} \mathbf{0} & \mathbf{0} \\ \mathbf{0} & \hat{\mathbf{K}}_3 + n\mathbf{K}_4 \end{bmatrix} + k^2 \begin{bmatrix} -\tilde{\mathbf{K}}_6 & \mathbf{0} \\ \mathbf{0} & \mathbf{K}_6 \end{bmatrix} \right) \begin{Bmatrix} \boldsymbol{\phi} \\ \mathbf{q} \end{Bmatrix} = \mathbf{0} \tag{39}$$

where the symmetry is retained. For implementation, it is convenient to apply the 'minus' sign to all matrices related to the fluid domain at the element definition stage.

If the coupling between the pipe and the external surrounding fluid is considered, the rows of the matrices in Eq. (39) need to be swapped.

2.5. Spectral elements for the discretisation of the cross-section

The choice of shape functions is of primary importance for modelling wave proagation. Using higher-order polynomials over non-uniformly spaced nodes, commonly referred to as spectral elements, offers several advantages over the typical SAFE implementation with linear or quadratic elements [27, 37, 38]. These include fast convergence and reduced size of the model. The details of the implementation of spectral finite elements for the discretisation of the axisymmetric cross-section are discussed in this section.

2.5.1. Gauss-Lobatto-Legendre nodes and Langrangian interpolants

One characteristic feature of spectral elements is that they use higher-order polynomials based on non-uniformly spaced nodes. The choice of the polynomial and the scheme for computing nodal location is application specific and more details can be found in relevant literature, e.g. [38]. A typical combination, used in this paper, is to employ Lagrange polynomials as shape functions over Gauss-Lobatto-Legendre (GLL) nodes. For axisymmetric domains we are using one-dimensional elements. Unlike for the conventional FE, the nodes now coincide with the integration points.

Let us start from defining the nodal locations as roots of the equation [39]

$$\left(1-\xi^2\right)\frac{\mathrm{d}P_N(\xi)}{\mathrm{d}\xi}=0 \tag{40}$$

where $P_N(\xi)$ is the Legendre polynomial of order N. These $(N+1)$ roots (ξ_i) can be identified numerically. For completeness, the weights for the GLL quadrature are defined as:

$$w_i=\begin{cases}\dfrac{2}{N(N+1)} & \text{if} \quad i=0 \quad \text{or} \quad i=N+1\\ \dfrac{2}{N(N+1)P_N(\xi_i)^2} & \text{otherwise}\end{cases} \tag{41}$$

For a given set of GLL nodes, we compute $(N+1)$ Lagrange interpolants of order N:

$$h_i(\xi)=\begin{cases}\displaystyle\prod_{j=1,i\neq j}^{N+1}\frac{\xi-\xi_j}{\xi_i-\xi_j} & \text{if} \quad i\neq j\\ 1 & \text{otherwise}\end{cases} \tag{42}$$

The derivatives of the interpolants are calculated as:

$$\frac{\mathrm{d}h_i(\xi)}{\mathrm{d}\xi}=\sum_{j=1,i\neq j}^{N+1}\frac{1}{\xi_i-\xi_j}\prod_{k=1,k\neq(i,j)}^{N+1}\frac{\xi-\xi_k}{\xi_i-\xi_k} \tag{43}$$

For one-dimensional elements, the Jacobian matrix describing the mapping form physical into natural coordinates has just one element:

$$\mathbf{J}=\begin{bmatrix}\frac{\mathrm{d}h_1}{\mathrm{d}\xi} & \frac{\mathrm{d}h_2}{\mathrm{d}\xi} & \dots & \frac{\mathrm{d}h_{N+1}}{\mathrm{d}\xi}\end{bmatrix}\begin{bmatrix}r_1 & r_2 & \dots & r_{N+1}\end{bmatrix}^\top \tag{44}$$

The determinant of the Jacobian matrix is denoted as $J\,(\det\mathbf{J}=J)$

2.5.2. Gauss-Lobatto-Jacobi (0, 1) nodes and weights for core elements

For axisymmetric domains, adopting GLL nodal locations and integration scheme results in the appearance of singular or undetermined terms at $r = 0$ (every element matrix has the form $\int \dots r \, \mathrm{d}r$). Since GLL points include $(-1, 1)$ coordinates, the element matrices need to be evaluated at $r = 0$, which corresponds to $\xi = -1$ for the element adjacent to the axis of symmetry (core element).

Several approaches have been proposed to overcome this difficulty. In this paper we follow e.g. [40–43] who suggested employing the Gauss-Lobatto-Jacobi (0, 1) (GLJ) scheme for determining node locations and integrating over the core element. The advantage of the GLJ quadrature is that it incorporates the radius in the weight allowing for eliminating the aforementioned numerical difficulty. A brief summary of the calculation of nodes and weights for the GLJ quadrature is given below. For detailed information, the reader is directed to literature related to spectral methods, e.g. [39].

We first define $x_{i,N}^{\alpha,\beta}$ as roots of a Jacobi polynomial $P_N^{\alpha,\beta}(x)$. These roots can be identified numerically, using a Newton-Raphson method. A very common algorithm is presented in Appendix B.2 of [39]. Of interest here is the (0, 1) quadrature, hence $\alpha = 0$ and $\beta = 1$. The node locations are defined as

$$\xi_i = \begin{cases} -1 & \text{for} \quad i = 1 \\ x_{i-1,N-2}^{1,2} & \text{for} \quad 1 < i < N+1 \\ 1 & \text{for} \quad i = N \end{cases} \tag{45}$$

whereas the associated weights as

$$w_i = \begin{cases} 2C_{1,N-2}^{0,1} & \text{for} \quad i = 1 \\ C_{i,N-2}^{0,1} & \text{for} \quad 1 < i < N \\ C_{N-1,N-2}^{0,1} & \text{for} \quad i = N \end{cases} \tag{46}$$

where

$$C_{i,N-2}^{0,1} = \frac{2^2 \Gamma(N)\Gamma(N+1)}{(N-1)(N-1)!\Gamma(N+2)\left[P_{N-1}^{0,1}(\xi_i)\right]^2} \tag{47}$$

with $\Gamma(x)$ being the generalised factorial.

The Langrangian interpolants through the nodes given above are defined as

$$h_i(\xi) = \begin{cases} \dfrac{2(-1)^{N-1}(\xi-1)\left[P_{N-1}^{0,1}(\xi)\right]'}{(N-1)N(N+1)} & \text{for} \quad i=1 \\ \dfrac{(\xi^2-1)\left[P_{N-1}^{0,1}(\xi)\right]'}{(N-1)(N+1)P_{N-1}^{0,1}(\xi_i)(\xi-\xi_i)} & \text{for} \quad 1<i<N \\ \dfrac{(1+\xi)\left[P_{N-1}^{0,1}(\xi)\right]'}{(N-1)(N+1)} & \text{for} \quad i=N \end{cases} \tag{48}$$

2.5.3. Avoiding undetermined terms

The integrations of the axisymmetric element matrices can be written in a general form

$$\int_r f(r) r \, \mathrm{d}r \tag{49}$$

Let us rewrite this integral in the natural coordinates (with respect to GLJ nodes)

$$\int_{-1}^{1} f(\xi) \frac{r}{1+\xi} (1+\xi) J \, \mathrm{d}\xi \tag{50}$$

where J is the determinant of the Jacobian matrix. The term $(1+\xi)$ is absorbed in the weight, since the GLJ quadrature is defined as

$$\int_{-1}^{1} g(\xi)(1+\xi) \, \mathrm{d}\xi = \sum_{i=1}^{N+1} w_i g(\xi_i) \tag{51}$$

where ξ_i and w_i are GLJ nodes and weights, respectively. For the considered case $g(\xi) = f(\xi)\frac{r}{1+\xi}$. On the axis of symmetry the $\frac{r}{1+\xi}$ becomes undetermined since both r and $(1+\xi)$ tend to zero as ξ approaches -1. We evaluate this fraction using the de'Hospital's rule [40]

$$\left.\frac{r(\xi)}{1+\xi}\right|_{\xi=-1} = \left.\frac{\mathrm{d}r}{\mathrm{d}\xi}\right|_{\xi=-1} \tag{52}$$

From the finite element discretisation, $r(\xi) = \mathbf{N}(\xi)\mathbf{r}_i$, where $\mathbf{r}_i$ are r-coordinates of the nodes. Therefore,

$$\left.\frac{\mathrm{d}r}{\mathrm{d}\xi}\right|_{\xi=-1} = \left.\frac{\mathrm{d}\mathbf{N}(\xi)}{\mathrm{d}\xi}\right|_{\xi=-1} \mathbf{r}_i \tag{53}$$

which is equal to the one-element Jacobian matrix.

For implementation, it is convenient to scale the radius for core elements according to the node at which the matrices are evaluated [40]

$$r = \begin{cases} \dfrac{r}{1+\xi} & \text{if} \quad \xi \neq -1 \\ J & \text{if} \quad \xi = -1 \end{cases} \tag{54}$$

Another singularity arises when strains in a solid domain are computed on the axis of symmetry. In cylindrical coordinates, several components include division by r, for example u_r/r, or u_θ/r (for $n = 0$ circumferential order). We note, however that the boundary conditions on the axis of symmetry imply that both u_r and u_θ vanish. De'Hospital's rule can be applied again [43]

$$\left.\frac{u_r}{r}\right|_{\xi=-1} = \left[\left.\frac{\mathrm{d}r}{\mathrm{d}\xi}\right|_{\xi=-1}\right]^{-1} \left.\frac{\mathrm{d}u_r}{\mathrm{d}\xi}\right|_{\xi=-1} \tag{55}$$

where the z- and θ- dependence of the displacement has been dropped. Recalling that $u_r(\xi) = \mathbf{N}(\xi)\mathbf{u}_{\mathbf{r}i}$ we can write the derivative of the displacement as

$$\frac{\mathrm{d}u_r}{\mathrm{d}\xi} = J\mathbf{N}_{,r}\mathbf{u}_{\mathbf{r}i} \tag{56}$$

which finally yields

$$\left.\frac{u_r}{r}\right|_{\xi=-1} = \left.\mathbf{N}_{,r}\right|_{\xi=-1} \mathbf{u}_{\mathbf{r}i} \tag{57}$$

An analogous derivation applies to the $\frac{u_\theta}{r}$ component and all derivatives over θ. Recalling Eq. (8), where the FE formulation for strain was derived, we redefine strain for $\xi = -1$ the node in the core element located at the axis of symmetry as

$$\bar{\boldsymbol{\epsilon}}\Big|_{\xi=-1} = \left(\mathbf{L}\mathbf{N}_{,r} + \mathbf{L}_r\mathbf{N}_{,r} + \mathbf{L}_\theta\mathbf{N}_{,r}\frac{\partial}{\partial\theta} + \mathbf{L}_z\mathbf{N}\frac{\partial}{\partial z}\right)\bar{\mathbf{q}} \tag{58}$$

The aforementioned solutions allow for avoiding singular and undetermined terms in element matrices making the use of spectral elements in axisymmetric domains feasible.

3. Perfectly matched layer in SAFE

In this section the implementation of a perfectly matched layer (PML) in SAFE is presented. PMLs are of great use for modelling waves in structures embedded

in a restraining medium. PML maps the original geometry into a new coordinate system which both 'stretches' the original geometry and attenuates the waves (as the new coordinate is complex). The SAFE-PML elements are derived in the same way as the 'standard' elements described in Sec. 2.1 and Sec. 2.3, the only difference being that the calculations are performed in the new, 'stretched' domain. The new coordinate $\tilde{r}(r)$ is defined as

$$\tilde{r}(r) = \int_0^r \gamma(\xi)\,\mathrm{d}\xi \tag{59}$$

where γ is a stretching function which defines the PML profile. To achieve a desired effect, the stretching function must attenuate the waves which is achieved by using a complex coordinate. It is known that for embedded waveguides, the wave that decays in the z-direction ($\mathrm{Im}(k) < 0$), grows in the r direction ($\mathrm{Im}(k_r) > 0$, where k_r is the projection of the wavenumber onto the r-direction). For the PML to be effective, the new coordinate $\tilde{r}$ must make the component $\mathrm{e}^{-\jmath k_r \tilde{r}}$ decay, that is $\mathrm{Im}(\tilde{r}) < -\mathrm{Im}(k_r)$.

There are a number of variants to choose for the γ function. Two have received attention in the vibroacoustic community, namely a polynomial [25–27] and an exponential [28] profile. The latter seems to align better with the physical intuition and according to [28] outperforms the polynomial counterpart for most cases. The exponential profile is defined as

$$\gamma(r) = \begin{cases} 1 & r \le d \\ \mathrm{e}^{a\frac{r-d}{h}} - \jmath\left(\mathrm{e}^{b\frac{r-d}{h}} - 1\right) & r > d \end{cases} \tag{60}$$

where a and b are the parameters of the profile. An average value of of the PML profile along its length provides a useful measure for evaluating its characteristics and will be exploited for determining optimal PML parameters.

$$\hat{\gamma} = \frac{1}{h}\int_d^{d+h} \gamma(r)\,\mathrm{d}r = \frac{\mathrm{e}^a - 1}{a} + \jmath\frac{b - \mathrm{e}^b + 1}{b} \tag{61}$$

The transformed stretched coordinate can be found from a closed-form expression:

$$\tilde{r}(r_i) = \int_0^{r_i} \gamma(\xi)\,\mathrm{d}\xi = d + \frac{h}{a}\left(\mathrm{e}^{a\frac{r_i-d}{h}} - 1\right) - \jmath h\left(\frac{1}{b}\mathrm{e}^{b\frac{r_i-d}{h}} - \frac{1}{b} - r_i\right) \tag{62}$$

Below, we show the modifications to element matrices for PML elements. The change of variables $\tilde{r} \mapsto r$ implies that for any function $\tilde{f}$:

$$\frac{\partial \tilde{f}}{\partial \tilde{r}} = \frac{1}{\gamma}\frac{\partial f}{\partial r}, \qquad \mathrm{d}\tilde{r} = \gamma \mathrm{d}r \tag{63}$$

In fact, this transformation is the only change to the SAFE matrices derived in the preceding sections. Both the form of the SAFE governing equation and the global matrices assembly process remain the same as for elements in physical coordinates. Nevertheless, the respective element matrices are written explicitly below, for completeness.

3.1. Structural PML element

Applying the coordinate stretching transformation to Eq. (11) yields

$$\begin{aligned}
\mathbf{K}_1 &= 2\pi \int_{r_0}^{r_1} \tilde{\mathbf{B}}_1^\top \mathbf{C} \tilde{\mathbf{B}}_1 \tilde{r}\gamma \,\mathrm{d}r \qquad & \mathbf{K}_{f1} &= 2\pi \int_{r_0}^{r_1} \mathbf{B}_3^\top \mathbf{C} \tilde{\mathbf{B}}_1 \tilde{r}\gamma \,\mathrm{d}r \\
\mathbf{K}_{f2} &= 2\pi \int_{r_0}^{r_1} \tilde{\mathbf{B}}_2^\top \mathbf{C} \tilde{\mathbf{B}}_1 \tilde{r}\gamma \,\mathrm{d}r \qquad & \mathbf{K}_{f3} &= 2\pi \int_{r_0}^{r_1} \tilde{\mathbf{B}}_2^\top \mathbf{C} \mathbf{B}_3 \tilde{r}\gamma \,\mathrm{d}r \\
\mathbf{K}_2 &= \mathbf{K}_{f2} - \mathbf{K}_{f2}^\top & \mathbf{K}_3 &= \mathbf{K}_{f1} - \mathbf{K}_{f1}^\top \\
\mathbf{K}_4 &= \mathbf{K}_{f3}^\top - \mathbf{K}_{f3} & \mathbf{K}_5 &= 2\pi \int_{r_0}^{r_1} \tilde{\mathbf{B}}_2^\top \mathbf{C} \tilde{\mathbf{B}}_2 \tilde{r}\gamma \,\mathrm{d}r \\
\mathbf{K}_6 &= 2\pi \int_{r_0}^{r_1} \mathbf{B}_3^\top \mathbf{C} \mathbf{B}_3 \tilde{r}\gamma \,\mathrm{d}r \qquad & \mathbf{M} &= 2\pi\rho \int_{r_0}^{r_1} \mathbf{N}^\top \mathbf{N} \tilde{r}\gamma \,\mathrm{d}r
\end{aligned} \tag{64}$$

with

$$\tilde{\mathbf{B}}_1 = \frac{1}{\tilde{r}}\mathbf{L}\mathbf{N} + \frac{1}{\gamma(r)}\mathbf{L}_r \mathbf{N}_{,r} \qquad \text{and} \qquad \tilde{\mathbf{B}}_2 = \frac{1}{\tilde{r}}\mathbf{L}_\theta \mathbf{N} \tag{65}$$

When calculating the integrals using the Gauss quadrature, both the stretching function γ and the transformed coordinate $\tilde{r}$ are evaluated at each integration point.

3.2. Acoustic PML element

Along the same lines, respective matrices for the acoustic PML element are dervied:

$$\begin{aligned}
\mathbf{M} &= \int_{r_0}^{r_1} \frac{1}{c^2} \mathbf{N}_\phi^\top \mathbf{N}_\phi \gamma \tilde{r} \,\mathrm{d}r \qquad & \mathbf{K}_1 &= \int_{r_0}^{r_1} \frac{1}{\gamma^2} \mathbf{N}_{\phi,r}^\top \mathbf{N}_{\phi,r} \gamma \tilde{r} \,\mathrm{d}r \\
\mathbf{K}_5 &= \int_{r_0}^{r_1} \frac{1}{\tilde{r}^2} \mathbf{N}_\phi^\top \mathbf{N}_\phi \gamma \tilde{r} \,\mathrm{d}r & \mathbf{K}_6 &= \int_{r_0}^{r_1} \mathbf{N}_\phi^\top \mathbf{N}_\phi \gamma \tilde{r} \,\mathrm{d}r
\end{aligned} \tag{66}$$

The matrices are integrated in the same way as it is done for structural elements.

3.3. The choice of the PML parameters and meshing

The physical implications of the geometrical parameters of the PML as well as the average value of the stretching function $g\hat{a}\hat{m}ma(r)$ are explained in detail in excellent discussions by Treyssède [25] and Nguyen et al. [26]. Their main observations and summarised below for the sake of completeness:

- the further d is from the waveguide of interest (i.e. pipe, rod, etc.), the more the radiated waves are allowed to grow before they enter the PML, which then requires more effort to damp them down. Hence, d should be set as close as possible to the waveguide. In this paper, we always set the PML directly adjacent to the waveguide.

- The imaginary part of $\hat{\gamma}$ determines 'how far' into the imaginary part of the wavenumber spectrum will the PML penetrate. Given the condition for waves to decay in the PML, the larger the negative imaginary part is, the more leaky waves can be found.

- The absorption across the PML is determined by $|\hat{\gamma}|h$ product. Absorption can be enhanced by either increasing the modulus of $\hat{\gamma}$ or by making the PML thicker. However, the trade-off between the two exists. The former may not lead to satisfactory results if the wave decay is too abrupt and cannot be well represented by the mesh. The latter requires discretisation of a larger geometry and, consequently, the increase of the size of the model.

Based on these observations, we formulated several criteria that allow for determining optimal parameters of the PML for a chosen configuration *a priori*, minimising the need for manual tuning. In general, two limiting cases define the effectiveness of the PML, namely the long wavelength and the short wavelength limits. In the former, the challenge is to capture leaky waves when the wavelength in the surrounding medium is long and it is difficult to achieve attenuation with reasonably thin PMLs. The latter requires a careful consideration of the mesh density as one of the effects of the PML is to shorten the wavelength.

We first discuss the short wavelength limit referring to the highest frequency of interest. One starts from computing the 'largest' radial wavenumber, which can be done from bulk wavespeeds in the waveguide and in the surrounding medium and the maximum allowed attenuation:

$$k_{r\,\max} = \sqrt{k_b^2 - k_w^2} - \jmath k_{\mathrm{im}\,\max} \tag{67}$$

One should choose a combination of the two that gives the radial wavenumber with the largest real part. The exponential profile used in this paper is controlled by two parameters: a, which is predominantly responsible for shortening the wavelength, and b which governs attenuation. The choice of values for these is somewhat arbitrary, but the experience of the authors shows that it is best if b is slightly larger than a and that a reasonable range for these parameters is between 2 and 8. The chosen profile performs very well for $a = 6$ and $b = 7$ and these values were kept for all simulations.

Having chosen a and b, one can calculate the 'shortened' wavelength in the PML. Recalling that the harmonic variation of displacement along r is of the form $\mathrm{e}^{-\jmath k_r r}$, one can calculate the equivalent wavenumber by substituting the maximum wavenumber $k_{r\,\max}$ and the stretched radial coordinate from Eq. (62). The wavelength is the shortest at the end of the PML ($r = d + h$), hence one writes

$$\mathrm{e}^{-\jmath k_{r\,\max}\tilde{r}} = \mathrm{e}^{-\jmath[\mathrm{Re}(k_{r\,\max})+\jmath\mathrm{Im}(k_{r\,\max})]\left[d+\frac{h}{a}(\mathrm{e}^a-1)-\jmath\left(\frac{h}{b}\left(\mathrm{e}^b-1\right)\right)+\jmath h\right]} \tag{68}$$

The above equation can be mapped to the form $\mathrm{e}^{-\jmath k_{\mathrm{PML}}(d+h)}$ which allows for determining the equivalent wavenumber at the PML termination. Although the actual expression is rather formidable (and hence not presented here), it can be well approximated using just one term

$$k_{\mathrm{PML}} \approx \frac{h}{d+h} k_{r\mathrm{max}} \frac{\mathrm{e}^{a-1}}{a} \tag{69}$$

Next, it is necessary to specify the number of 'shortened' wavelengths inside the PML. The experience suggests that somewhere between 2 and 5 both provides accurate results and avoids incurring excessive computational costs. Although two wavelengths will suffice for most applications, choosing a larger number enhances the performance of the PML at lower frequencies and is strongly encouraged.

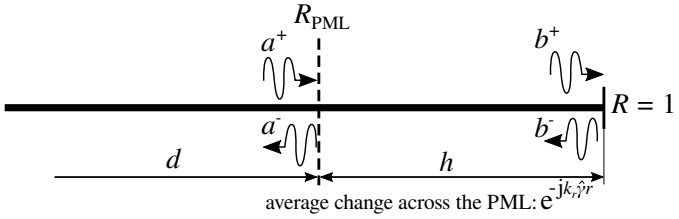

Figure 2: Schematic diagram for the calculation of the PML reflection coefficient R_{PML}.

Knowing the smallest shortened wavelength in the PML, its physical thickness can be calculated from a simple quadratic equation

$$\frac{2\pi}{\frac{h}{d+h}k_{\mathrm{PML}}} = ch \tag{70}$$

where c is the desired number of wavelengths.

At high frequencies, the mesh density becomes critical for reflection-free performance of the PML. A criterion developed by Gravenkamp [29] is adopted here, with slight reformulations. Recalling that it has been chosen to include c wavelengths within the PML, the order of the GLL element should be $(\pi c + 3)$ (note that the number of nodes is n + 1). The equations presented above allow for determining the optimal thickness of the PML and mesh parameters only from the geometry of the waveguide and material properties.

A very advantageous characteristic of the presented formulation is that it is capable of capturing leaky waves at very low frequencies, i.e. where the wavelengths in the surrounding medium are long. This is uncommon for PML applications. Most other numerical methods for embedded waveguides discussed in the introduction (see e.g. [19]) do not address the low frequency range. The evaluation of the PML performance at the long wavelength limit can be done in two ways. The first could be to follow a procedure analogous to that presented above. One would calculate the radial wavenumber at a low frequency by selecting bulk wavenumbers for the embedded medium and the waveguide that give the longest radial wavelength. The required thickness and mesh density of the PML could then be determined. However, we note that such set of parameters will be insufficient at high frequencies, where the wavelengths in the PML are markedly shorter. Only increasing mesh den-

sity could lead to satisfactory performance but at the same time would incur high computational costs. An alternative is to evaluate the performance of the short-wavelength limit PML by calculating the reflection coefficient at low frequencies and make small adjustments if necessary. A schematic diagram for this calculation is shown in Fig. 2. We assume that the reflection coefficient at the end of the PML is 1 (one wave type at a time, no mode conversion). Wave amplitude returning from the PML into the waveguide can be calculated as

$$a^- = a^+ \mathrm{e}^{-2\jmath k_r \hat{\gamma} h} \tag{71}$$

and the reflection coefficient from the PML as

$$R_{\mathrm{PML}} = \frac{a^-}{a^+} = \mathrm{e}^{-2\jmath k_r \hat{\gamma} h} \tag{72}$$

Of interest here is the magnitude of the reflection coefficient, which can be conveniently expressed as

$$|R_{\mathrm{PML}}| = \mathrm{e}^{\mathrm{Im}(2k_r \hat{\gamma} h)} \tag{73}$$

Substituting Eq. (61) from $\hat{\gamma}$ we obtain

$$|R_{\mathrm{PML}}| = \mathrm{e}^{2h\mathrm{Im}(k_r)\frac{\mathrm{e}^a - 1}{a}} \mathrm{e}^{2h\mathrm{Re}(k_r)\frac{b - \mathrm{e}^b + 1}{b}} \tag{74}$$

Such verifications performed by the authors showed that the exponential PMLs optimised for high frequency applications often work at low frequency if the number of shortened wavelengths (c) is taken as larger than two.

4. Governing equations and solution

4.1. Linearisation and solution

The quadratic eigenvalue problem from Eq. (17) is commonly solved by linearisation

$$(\mathbf{A} - k\mathbf{B})\hat{\boldsymbol{\psi}} = \mathbf{0} \tag{75}$$

A variety of linearisation schemes are available. We aimed at choosing one that allows for the symmetry of the system to be retained and renders **B** matrix invertible.

The following form fulfils the above

$$\left(\begin{bmatrix} \mathbf{K}_6 & \mathbf{0} \\ \mathbf{0} & -\left(\mathbf{K}_1 + n\hat{\mathbf{K}}_2 + n^2\mathbf{K}_5 - \omega^2\mathbf{M}\right) \end{bmatrix} - k \begin{bmatrix} \mathbf{0} & \mathbf{K}_6 \\ \mathbf{K}_6 & \hat{\mathbf{K}}_3 + n\mathbf{K}_4 \end{bmatrix} \right) \begin{Bmatrix} k\psi \\ \psi \end{Bmatrix} = \mathbf{0} \quad (76)$$

The solutions can be found efficiently by recasting the above equation to a standard eigenvalue problem $\left(\mathbf{B}^{-1}\mathbf{A} - k\mathbf{I}\right)\hat{\psi} = \mathbf{0}$ with $\mathbf{A}$ and $\mathbf{B}$ defined above. Note that $\mathbf{B}^{-1}$ needs to be computed only once, as it is independent of frequency. The structure of the matrices enables the shift-invert mode of sparse eigensolvers to be used. However, the axisymmetric assumption and the use of spectral elements usually render small problems, for which the full eigensolution is more efficient. Finally, owing to the symmetry of the system, left eigenvectors $\hat{\upsilon}$ are the same as the right eigenvectors $\hat{\psi}$, which is useful for calculating the real reciprocity relation [44] or the forced response.

The solution of Eq. (76) yields $2n$ eigenvalues and $2n$ eigenvectors corresponding to wavenumbers and wave mode shapes, respectively (if the full solution is used). Positive going waves may be identified by verifying whether $|e^{-\jmath k\Delta}|$ is smaller than one (with Δ being a small distance as compared to the wavelength). SAFE formulation provides elegant expressions for a number of quantities of interest for guided wave problems. The time-averaged kinetic energy can be calculated as

$$E_k = \frac{\omega^2}{4}\psi^{*\top}\mathbf{M}\psi \quad (77)$$

The time-averaged potential energy can be obtained from

$$E_p = \frac{1}{4}\psi^{*\top}\left(\mathbf{K}_1 + \jmath n\mathbf{K}_2 + n^2\mathbf{K}_5 + \jmath k^*\mathbf{K_F} - \jmath k\mathbf{K_F}^\top + kn\mathbf{K}_{Ft}^\top + k^* n\mathbf{K}_{ft} + kk^*\mathbf{K_6}\right)\psi \quad (78)$$

The component of the Poynting vector along the direction of propagation, corresponding to the power flow density, is evaluated from

$$P = \frac{-\omega}{2}\mathrm{Im}\left(\psi^{*\top}\left(\mathbf{K}_F - \jmath n\mathbf{K}_{Ft} - \jmath k\mathbf{K}_6\right)\psi\right) \quad (79)$$

And finally, the energy velocity can be calculated using the above mentioned quantities as:

$$c_E = \frac{P}{E_p + E_k} \quad (80)$$

For embedded waveguides, the energies, power and energy velocity are calculated from the subvectors and submatrices corresponding to the degrees of freedom of the core waveguide only.

4.2. Mode sorting

The numerical eigenvalue routine used to solve the SAFE governing equation returns the solutions unordered and any physical interpretation must be preceded by some kind of sorting routine. The most straightforward approach is to use the biorthogonality relation

$$\hat{\boldsymbol{\upsilon}}_i^{\top} \mathbf{B} \hat{\boldsymbol{\psi}}_j = b_j \delta_{ij} \tag{81}$$

Since the left and right eigenvectors are the same for the considered problems, calculating Eq. (81) at two adjacent frequencies allows for determining the similarity between particular wave solutions. It is convenient to normalise the eigenvectors with respect to Eq. (81) after the eigensolution and before mode sorting. Any two eigenvectors at neighbouring frequencies for which $\hat{\boldsymbol{\psi}}_i^{\top}(\omega_{i-1})\mathbf{B}\hat{\boldsymbol{\psi}}_j(\omega_i)$ is one or close two one correspond to the same dispersion curve.

SAFE models typically return a large number of wave solutions, of which only a small number corresponds to propagating waves. Moreover, for embedded waveguides, one needs to discern between guided waves and radiation waves (oscillating within the PML), which are of no interest. For the former, an arbitrary maximum allowable attenuation can be set corresponding to te application of interest. The latter can be achieved using an energy criterion as proposed in [25], where a ratio between kinetic energies in the PML and the whole waveguide was used to calculate an energy ratio

$$\eta = \frac{|E_{\text{PML}}|}{|E_{\text{total}|}} \tag{82}$$

where the magnitudes have been taken as the energies are complex in the stretched domain. The value of η is set arbitrarily, most often around 0.9 [26, 28].

5. Forced response

The calculation of the response of the structure to either acoustic or structural excitation is described in this section. The excitation is defined as a generalised

force vector $\bar{\mathbf{f}}(r,\theta,z,t) = \mathbf{f}(r,\theta,z)\mathrm{e}^{\jmath\omega t}$, where the time-harmonic factor is omitted hereafter for brevity. Its variation along the θ direction is expressed using a Fourier series

$$\mathbf{f}(r,\theta,z) = \sum_{0}^{\infty} \mathbf{f}_n(r,z)\mathrm{e}^{-\jmath n\theta} \tag{83}$$

while along z it is transformed into the wavenumber domain via a spatial Fourier transform

$$\tilde{\mathbf{f}}_n(r) = \int_{-\infty}^{\infty} \mathbf{f}_n(r,z)\mathrm{e}^{\jmath kz}\,\mathrm{d}z \tag{84}$$

Let us now recall the linearised form of the governing equation and add source terms on the right hand side

$$\left(\begin{bmatrix} \mathbf{K}_6 & \mathbf{0} \\ \mathbf{0} & -\left(\mathbf{K}_1 + n\hat{\mathbf{K}}_2 + n^2\mathbf{K}_5 - \omega^2\mathbf{M}\right) \end{bmatrix} - k \begin{bmatrix} \mathbf{0} & \mathbf{K}_6 \\ \mathbf{K}_6 & \hat{\mathbf{K}}_3 + n\mathbf{K}_4 \end{bmatrix} \right) \begin{Bmatrix} k\tilde{\mathbf{q}}_n \\ \tilde{\mathbf{q}}_n \end{Bmatrix} = \begin{Bmatrix} \mathbf{0} \\ \tilde{\mathbf{f}}_n \end{Bmatrix} \tag{85}$$

where $\tilde{\mathbf{q}}_n$ and $\tilde{\mathbf{f}}_n$ are the generalised displacement and generalised force vectors for circumferential order n, respectively (containing both acoustic and structural terms). The displacement can be written as an expansion in terms of propagating waves

$$\tilde{\mathbf{q}}_n = \mathbf{\Psi}_n \tilde{\mathbf{a}}_n \tag{86}$$

where $\mathbf{\Psi}$ is a matrix whose columns are the wave mode shapes and $\tilde{\mathbf{a}}$ is a vector of wave amplitudes in the k-domain. We rewrite Eq. (85) for a single wave i with simplified notation as

$$(\mathbf{A} - k\mathbf{B})\hat{\boldsymbol{\psi}}_{(n,i)}\tilde{a}_{(n,i)} = \begin{Bmatrix} \mathbf{0} \\ \tilde{\mathbf{f}}_n \end{Bmatrix} \tag{87}$$

and pre-multiply it by the transpose of $\boldsymbol{\psi}_i$ which, owing to the symmetry of the eigensystem, is also its left eigenvector

$$\hat{\boldsymbol{\psi}}_{(n,i)}^{\top}\mathbf{A}\hat{\boldsymbol{\psi}}_{(n,i)} - k\hat{\boldsymbol{\psi}}_{(n,i)}^{\top}\mathbf{B}\hat{\boldsymbol{\psi}}_{(n,i)}\tilde{a}_{(n,i)} = \hat{\boldsymbol{\psi}}_{(n,i)}^{\top} \begin{Bmatrix} \mathbf{0} \\ \tilde{\mathbf{f}}_n \end{Bmatrix} \tag{88}$$

At this point we can benefit from the normalisation of the eigenvectors with respect to the biorthogonality relation, which allows for simplyfying the above equation

and deriving an expression for the wave amplitudes

$$\tilde{a}_{(n,i)}(k) = \frac{1}{k_{(n,i)} - k} \hat{\boldsymbol{\psi}}^{\top}_{(n,i)} \begin{Bmatrix} \mathbf{0} \\ \tilde{\mathbf{f}}_n \end{Bmatrix} \tag{89}$$

As an illustration, we consider a point excitation at (r_f, θ_f, z_f)

$$\mathbf{f}(r, \theta, z) = \mathbf{f}_{\text{ext}} \delta(\theta - \theta_f) \delta(z - z_f) \tag{90}$$

where $\mathbf{f}_{\text{ext}}$ is the distribution of force along the r direction. Following [18], to avoid numerical problems, we substitute $\delta(\theta - \theta_f)$ with a narrow rectangular box function of width θ_0, which is taken very small. To retain unit load, the magnitude of the box function must be $(2\theta_0 r_f)^{-1}$. The Fourier coefficients for the expansion along θ can then be calculated as

$$\mathbf{f}_n = \frac{1}{2\pi} \int_0^{2\pi} \frac{1}{2\theta_0 r_f} \mathrm{e}^{\jmath k z_f} = \frac{1}{2\pi r_f} \frac{\sin n\theta_0}{n\theta_0} \tag{91}$$

Substituting the above into Eq. (89), one obtains

$$\tilde{a}_{(n,i)}(k) = \frac{1}{2\pi r_f} \frac{\sin n\theta_0}{n\theta_0} \frac{1}{k_{(n,i)} - k} \hat{\boldsymbol{\psi}}^{\top}_{(n,i)} \begin{Bmatrix} \mathbf{0} \\ \mathbf{f}_{\text{ext}} \end{Bmatrix} \mathrm{e}^{\jmath k z_f} \tag{92}$$

Wave amplitudes in physical coordinates are calculated by applying the inverse Fourier transform to the above equation

$$\tilde{a}_{(n,i)}(z) = \frac{1}{2\pi} \int_{-\infty}^{\infty} \frac{1}{2\pi r_f} \frac{\sin n\theta_0}{n\theta_0} \frac{1}{k_{(n,i)} - k} \hat{\boldsymbol{\psi}}^{\top}_{(n,i)} \begin{Bmatrix} \mathbf{0} \\ \mathbf{f}_{\text{ext}} \end{Bmatrix} \mathrm{e}^{\jmath k z_f} \mathrm{e}^{-\jmath k z} \, \mathrm{d}z \tag{93}$$

The integral is evaluated with the aid of the Cauchy residue theorem, with integration contours taken appropriately to the sign of the wavenumber k. For positive-going waves we obtain

$$\tilde{a}^{+}_{(n,i)}(z) = \frac{\jmath \sin n\theta_0}{2\pi r_f n\theta_0} \hat{\boldsymbol{\psi}}^{+,\top}_{(n,i)} \begin{Bmatrix} \mathbf{0} \\ \mathbf{f}_{\text{ext}} \end{Bmatrix} \mathrm{e}^{-\jmath k^{+}_{(n,i)}(z - z_f)} \tag{94}$$

The negative-going waves amplitudes are

$$\tilde{a}^{-}_{(n,i)}(z) = \frac{-\jmath \sin n\theta_0}{2\pi r_f n\theta_0} \hat{\boldsymbol{\psi}}^{-,\top}_{(n,i)} \begin{Bmatrix} \mathbf{0} \\ \mathbf{f}_{\text{ext}} \end{Bmatrix} \mathrm{e}^{-\jmath k^{-}_{(n,i)}(z - z_f)} \tag{95}$$

Having found the excited wave amplitudes, one can finally calculate the displacement/velocity potential response to the right of the excitation as

$$\mathbf{q}^{+}(\theta, z_r) = \mathbf{\Psi}^{+}\mathbf{a}_n^{+}(z_r) \tag{96}$$

6. Numerical verification - high frequency

In this section we validate the formulation developed in this paper with results from published literature. The purpose of the comparison is to demonstrate the accuracy and efficiency of the proposed approach. Three high-frequency cases have been chosen from the literature: (i) a circular steel rod in concrete [19, 26, 28], (ii) titanium rod in oil [31] and water-filled copper pipe in water [45].

6.1. Steel rod in concrete

A circular steel rod with 0.01 m radius embedded in concrete is considered first. This configuration has been studied by a number of researchers to date, two of which [26, 28] employed perfectly matched layers with SAFE. The PML was set to start at the interface between the rod and the concrete ($d = 0.01$ m) and respective material properties are given in Tab. 1. According to the criteria presented in Sec. 3.3, the PML thickness was set to 0.00286 m and meshed with an element of order 13, which allowed for including three shortened PML wavelengths at the highest frequency of interest with $a = 6$ and $b = 7$. The results are presented in Fig. 3 and with regard to the aforementioned references [19, 26, 28], they show in excellent agreement. One characteristic feature pointed out by the aforementioned authors is the discontinuity of L(0, 1) and F(2, 1) dispersion curves around the apparent crossing with longitudinal bulk wavespeed in concrete. This phenomenon is attributed to a change in the leakage pattern when the longitudinal waves cease to be radiated, owing to the Snell's law. It is worth noting that computing the solution at a single frequency step (including sorting of the waves) took around 16.5 ms (as compared to 1.31 s reported in [28]).

Table 1: Material properties and geometrical parameters for the steel rod in concrete case study (taken from [19])

material	c_L, km/s	c_S , km/s	ρ, kg m^{-3}
steel	5960	3260	7932
concrete	4222.1	2637.5	2300

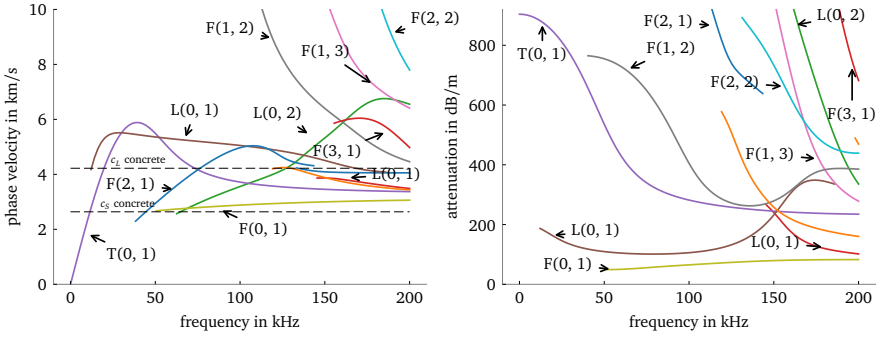

Figure 3: Phase velocity and attenuation for a steel rod embedded in concrete (the first three circumferential orders) [26]; only solutions with $\eta < 0.9$ and $|\mathrm{Im}(k)| < 200$ are shown.

Table 2: Material properties and geometrical parameters for the titanium rod in oil case study (taken from [31])

material	c_L, km/s	c_S , km/s	ρ, kg m^{-3}
titanium	6064.5	3230	4460
oil	1740	-	870

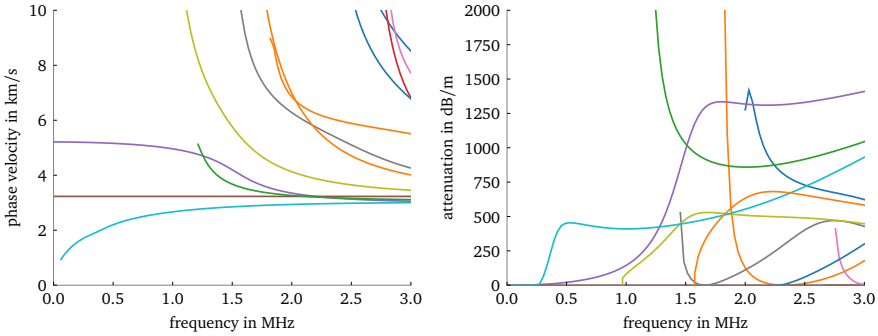

Figure 4: Phase velocity and attenuation for a titanium rod submerged in motor oil (the first three circumferential orders) [31]; only solutions with $\eta < 0.97$ and $|\mathrm{Im}(k)| < 350$ are shown.

6.2. Titanium rod in oil

The second example, titanium rod in oil as considered by Granvenkamp et al. [31], allows for demonstrating the structural-acoustic coupling implemented in the presented formulation. A circular rod of radius 1 mm is embedded in oil (material properties given in Tab. 2). As before, the PML is set to start at the boundary between the two materials and its thickness is calculated at 0.18 mm (the order of the PML spectral element is 13). The results are presented in Fig. **??** and, again, are found to be in very good agreement with [31]. The solution time for one frequency step (including wave sorting) was 7.7 ms.

6.3. Water-filled copper pipe submerged in water

The final numerical example is inspired by [45], who considered waves in a water-filled copper pipe with inner radius of 6.8 mm and wall thickness 0.7 mm.

Table 3: Material properties and geometrical parameters for the water-filled copper pipe in water case study (taken from [45])

material	c_L, km/s	c_S , km/s	ρ, kg m^{-3}
copper	4759	2325	8933
water	1500	-	1000

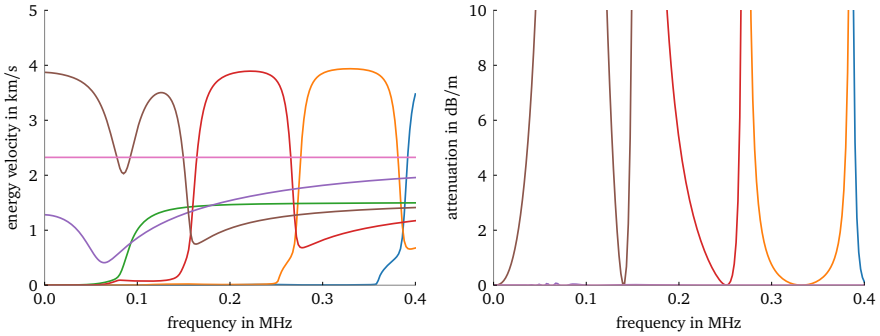

Figure 5: Energy velocity and attenuation for a water-filled copper pipe submerged in water ($n = 0$) [45]; only solutions with $\eta < 0.9$ and $|\mathrm{Im}(k)| < 100$ are shown.

Material properties are given in Tab. **??**. The PML was set to start at the boundary between the two materials, had thickness of 2.13 mm and was meshed with a spectral element of order 29. The solution time for one frequency step, including wave sorting was 16.8 ms. The results shown in Fig. 5 are in very good agreement with [45], with the exception that the energy velocity is plotted here. The fluid-dominated wave has nearly zero attenuation, unlike other identified solutions. One may notice small oscillations on the attenuation curve for the fluid-dominated wave between 0.06 and 0.1 MHz, where the energy velocity drops. Within this frequency range, the displacement decays in the PML so rapidly that it requires higher-order meshing. Increasing the number of desired 'shortened' PML wavelengths (see Sec. 3.3) helps to obtain more effective parameters for the PML (here, $c = 8$ was used).

7. Validation against experiments and an analytical model - low frequency

In this section we validate the developed model against low frequency measurements on a buried and a submerged water-filled plastic pipe. The low frequency regime is particularly challenging form the viewpoint of PMLs and although not very popular for non-destructive testing, it has demonstrated a strong potential for successful mapping and assessment of buried water pipes [46, 47].

7.1. Water-filled buried plastic pipe

First, we consider an MDPE pipe with the inner radius of 0.079 m and wall thickness 0.011 m. The pipe is filled with water and buried in a sandy soil at a depth of approximately 1 m. Respective material properties are given in Tab. **??**. Experimental wavenumbers are estimated from a number of hydrophones installed along the pipe. For the details of the experimental setup and data processing, the reader is referred to [9]. We note that only the fluid-dominated wave was captured in the experiment. In the model, the thickness of the PML was set to 0.02244 m and it was discretised with a spectral element of order 13. The solution time for one frequency step was 2.2 ms.

The results are presented in Fig. 6 and show very good agreement with the experimental data. Additionally, we plotted dispersion curves obtained from an analytical model developed for low frequency fluid-dominated waves with compact coupling with the soil [12]. The difference between the developed model and that from [12] becomes evident in the attenuation curve above 500 Hz. This can be attributed to several factors, the most important of which is that the analytical model does not consider loss related to shear effects in the pipe wall. It is also noted that it was difficult to extract the attenuation from the experiment above 500 Hz.

Additionally, we demonstrate the forced response calculation capability of the developed model. The excitation was assumed to be a point force acting on the outer pipe wall along the r direction, which corresponds to the type of excitation applied to the pipe in the experiment. Both the FRF and wave power distribution between the waves are computed and presented in Fig. 7 and Fig. 8, respectively.

Table 4: Material properties and geometrical parameters for the water-filled, buried MDPE pipe case study (taken from [9])

material	c_L, km/s	c_S , km/s	ρ, kg m^{-3}	loss factor
MDPE	2182.2	890.9	900	0.06
sandy soil	200	100	1500	-
water	1500	-	1000	-

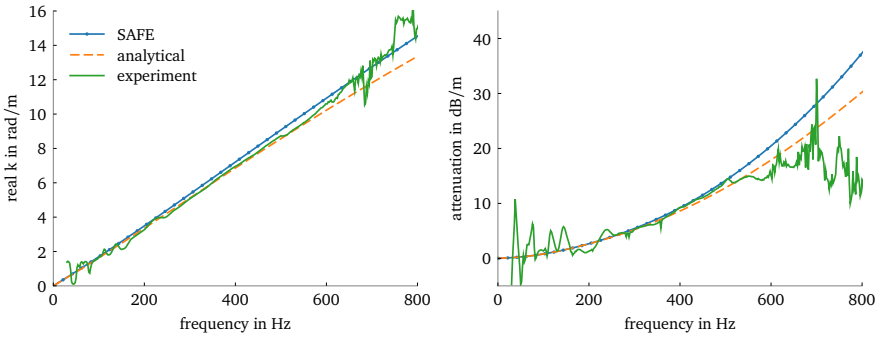

Figure 6: Wavenumber and attenuation for a water-filled MDPE pipe buried in soil (only the fluid-dominated wave); comparison between the present model, experiments [9] and an analytical model from [12].

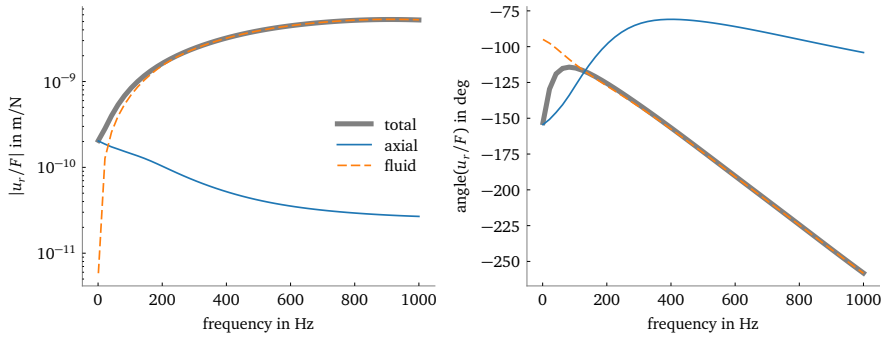

Figure 7: Predicted FRF (total and per wave) at 0.1 m from the excitation (point force directed radially towards the pipe axis at the outer surface of the pipe). The response is read at the same degree of freedom as the applied force.

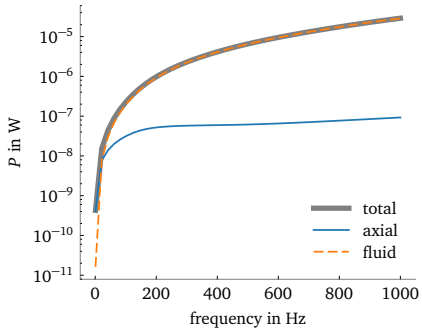

Figure 8: Predicted propagating wave power distribution (total and per wave) as a response to 1N point force directed radially towards the pipe axis at the outer surface of the pipe.

Two wave types are triggered with this excitation - the axial and the fluid-dominated wave. The fluid-dominated wave is shown to govern the response throughout the whole frequency range, with a very small contribution of the axial wave at low frequencies. This is confirmed in Fig. 8, where propagating wave power in response to a 1 N excitation is plotted.

7.2. Water-filled plastic pipe submerged in water

The last case study is for the same fluid-filled MDPE pipe, but this time - submerged in water. The details of experimental setup and data processing can be

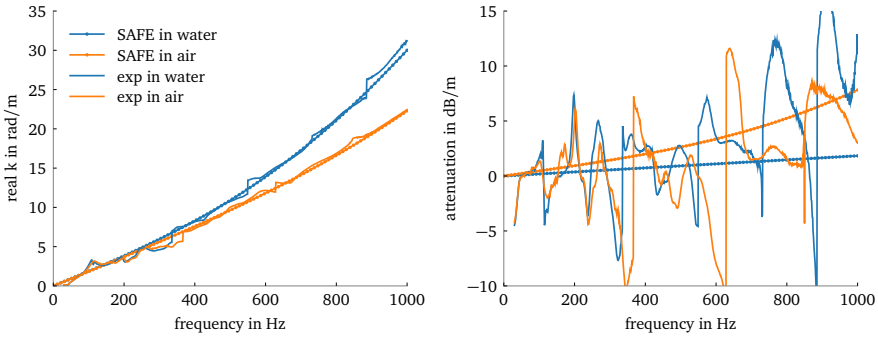

Figure 9: Wavenumber and attenuation for a water-filled MDPE pipe submerged in water (only the fluid-dominated wave); comparison between the present model and experiments[10].

found in [10]. Both the dimensions and the material properties are the same as for the buried case. The thickness of the PML was set to 0.1394 m and it was meshed with one spectral element of order 13. The solution time for a single frequency step including mode sorting was 1.6 ms. The comparison between the presented model and the experimental data is given in Fig. 9 showing very good agreement for the wavenumber. The attenuation curves could not be well resolved from the experiment owing to a failure of one of the sensors, as explained in [10].

8. Conclusions

A wave propagation model for axisymmetric fluid-filled embedded/submerged elastic waveguides was presented in this paper. It is based on the semi-analytical finite element principle, where only the cross-section is discretised using finite elements and spatial harmonicity of the displacement is assumed in the propagation direction. To enhance the efficiency of the solution, higher-order spectral elements were used and singularities at the axis of symmetry were circumvented by using Gauss-Lobatto-Jacobi (0, 1) quadrature for core elements. The surrounding medium, either structural or acoustic, was modelled using a perfectly matched layer with an exponential stretching function. A procedure for determining PML parameters and the element order from the geometry and material properties of the system

were derived and presented allowing for accurate predictions in both low and high frequency regimes, rather uncommon for PMLs. Finally, the validity of the model was demonstrated in three numerical verification cases against published results and two experimental case studies, all showing very good agreement. An implementation of the presented model in Python is made available with this article and relevant access details are given in the Acknowledgements section.

Acknowledgements

The authors gratefully acknowledge the support provided by the EPSRC (under grant EP/K021699/1). The data supporting this study are openly available from the University of Southampton repository at (DOI will be included upon acceptance). An implementation of the presented model in Python is available at (DOI will be included upon acceptance).

References

[1] M. J. S. Lowe, D. N. Alleyne, P. Cawley, Defect detection in pipes using guided waves, Ultrasonics 36 (1) (1998) 147–154. doi:10.1016/S0041-624X(97)00038-3.
URL http://www.sciencedirect.com/science/article/pii/S0041624X97000383

[2] J. L. Rose, A Baseline and Vision of Ultrasonic Guided Wave Inspection Potential, Journal of Pressure Vessel Technology 124 (3) (2002) 273–282.

[3] C. R. Fuller, F. J. Fahy, Characteristics of wave propagation and energy distributions in cylindrical elastic shells filled with fluid, Journal of Sound and Vibration 81 (4) (1982) 501–518. doi:10.1016/0022-460X(82)90293-0.
URL http://www.sciencedirect.com/science/article/pii/0022460X82902930

[4] J. Greenspon, Axially Symmetric Vibrations of a Thick Cylindrical Shell in an Acoustic Medium, The Journal of the Acoustical Society of America 32 (8)

(1960) 1017–1025. doi:10.1121/1.1908266.
URL http://asa.scitation.org/doi/10.1121/1.1908266

[5] B. Sinha, T. Plona, S. Kostek, S. Chang, Axisymmetric wave propagation in fluid-loaded cylindrical shells. I: Theory, The Journal of the Acoustical Society of America 92 (2) (1992) 1132–1143. doi:10.1121/1.404040.
URL http://asa.scitation.org/doi/abs/10.1121/1.404040

[6] K. Toki, S. Takada, Earthquake response analysis of underground tubular structure, Bulletin of the Disaster Prevention Research Institute 24 (2) (1974) 107–125.
URL http://repository.kulib.kyoto-u.ac.jp/dspace/handle/2433/124841

[7] A. N. Jette, J. G. Parker, Surface displacements accompanying the propagation of acoustic waves within an underground pipe, Journal of Sound and Vibration 69 (2) (1980) 265–274. doi:10.1016/0022-460X(80)90611-2.
URL http://www.sciencedirect.com/science/article/pii/0022460X80906112

[8] J. M. Muggleton, M. J. Brennan, R. J. Pinnington, Wavenumber prediction of waves in buried pipes for water leak detection, Journal of Sound and Vibration 249 (5) (2002) 939–954. doi:10.1006/jsvi.2001.3881.
URL http://www.sciencedirect.com/science/article/pii/S0022460X01938817

[9] J. M. Muggleton, M. J. Brennan, P. W. Linford, Axisymmetric wave propagation in fluid-filled pipes: wavenumber measurements in in vacuo and buried pipes, Journal of Sound and Vibration 270 (1–2) (2004) 171–190. doi:10.1016/S0022-460X(03)00489-9.
URL http://www.sciencedirect.com/science/article/pii/S0022460X03004899

[10] J. M. Muggleton, M. J. Brennan, Leak noise propagation and attenuation in submerged plastic water pipes, Journal of Sound and Vibration 278 (3)

(2004) 527–537. doi:10.1016/j.jsv.2003.10.052.
URL http://www.sciencedirect.com/science/article/pii/S0022460X03013270

[11] J. M. Muggleton, J. Yan, Wavenumber prediction and measurement of axisymmetric waves in buried fluid-filled pipes: Inclusion of shear coupling at a lubricated pipe/soil interface, Journal of Sound and Vibration 332 (5) (2013) 1216–1230. doi:10.1016/j.jsv.2012.10.024.
URL http://www.sciencedirect.com/science/article/pii/S0022460X12008255

[12] Y. Gao, F. Sui, J. M. Muggleton, J. Yang, Simplified dispersion relationships for fluid-dominated axisymmetric wave motion in buried fluid-filled pipes, Journal of Sound and Vibration 375 (2016) 386–402. doi:10.1016/j.jsv.2016.04.012.
URL http://www.sciencedirect.com/science/article/pii/S0022460X16300463

[13] J. M. Muggleton, M. Kalkowski, Y. Gao, E. Rustighi, A theoretical study of the fundamental torsional wave in buried pipes for pipeline condition assessment and monitoring, Journal of Sound and Vibration 374 (2016) 155–171. doi:10.1016/j.jsv.2016.03.035.
URL http://www.sciencedirect.com/science/article/pii/S0022460X16300104

[14] M. Lowe, Matrix Techniques for Modeling Ultrasonic Waves in Multilayered Media, IEEE Transactions on Ultrasonics, Ferroelectrics, and Frequency Control 42 (4) (1995) 525–542. doi:10.1109/58.393096.

[15] B. Pavlakovic, M. Lowe, D. Alleyne, P. Cawley, Disperse: A General Purpose Program for Creating Dispersion Curves, in: D. O. Thompson, D. E. Chimenti (Eds.), Review of Progress in Quantitative Nondestructive Evaluation, no. 16 in Review of Progress in Quantitative Nondestructive Evaluation, Springer US, 1997, pp. 185–192, dOI: 10.1007/978-1-4615-5947-4_24.

URL http://link.springer.com/chapter/10.1007/978-1-4615-5947-4_24

[16] B. Pavlakovic, Leaky Guided Ultrasonic Waves in NDT, PhD, Imperial College of Science, Technology and Medicine. University of London (1998).

[17] I. Bartoli, A. Marzani, F. Lanza di Scalea, E. Viola, Modeling wave propagation in damped waveguides of arbitrary cross-section, Journal of Sound and Vibration 295 (3-5) (2006) 685–707. doi:10.1016/j.jsv.2006.01.021.
URL http://linkinghub.elsevier.com/retrieve/pii/S0022460X06001179

[18] A. Marzani, Time-transient response for ultrasonic guided waves propagating in damped cylinders, International Journal of Solids and Structures 45 (25–26) (2008) 6347–6368. doi:10.1016/j.ijsolstr.2008.07.028.
URL http://www.sciencedirect.com/science/article/pii/S0020768308003089

[19] M. Castaings, M. Lowe, Finite element model for waves guided along solid systems of arbitrary section coupled to infinite solid media, The Journal of the Acoustical Society of America 123 (2) (2008) 696–708. doi:10.1121/1.2821973.
URL http://scitation.aip.org/content/asa/journal/jasa/123/2/10.1121/1.2821973

[20] H. Jia, M. Jing, J. Rose, Guided wave propagation in single and double layer hollow cylinders embedded in infinite media, The Journal of the Acoustical Society of America 129 (2) (2011) 691–700. doi:10.1121/1.3531807.
URL http://scitation.aip.org/content/asa/journal/jasa/129/2/10.1121/1.3531807

[21] M. Mazzotti, I. Bartoli, A. Marzani, E. Viola, A coupled SAFE-2.5d BEM approach for the dispersion analysis of damped leaky guided waves in

embedded waveguides of arbitrary cross-section, Ultrasonics 53 (7) (2013) 1227–1241. doi:10.1016/j.ultras.2013.03.003.
URL http://www.sciencedirect.com/science/article/pii/S0041624X13000668

[22] M. Mazzotti, I. Bartoli, A. Marzani, Ultrasonic leaky guided waves in fluid-coupled generic waveguides: hybrid finite-boundary element dispersion analysis and experimental validation, Journal of Applied Physics 115 (14) (2014) 143512. doi:10.1063/1.4870857.
URL http://scitation.aip.org/content/aip/journal/jap/115/14/10.1063/1.4870857

[23] M. Mazzotti, I. Bartoli, G. Castellazzi, A. Marzani, Computation of leaky guided waves dispersion spectrum using vibroacoustic analyses and the Matrix Pencil Method: A validation study for immersed rectangular waveguides, Ultrasonics 54 (7) (2014) 1895–1898. doi:10.1016/j.ultras.2014.05.009.
URL http://www.sciencedirect.com/science/article/pii/S0041624X14001279

[24] J.-P. Berenger, A perfectly matched layer for the absorption of electromagnetic waves, Journal of Computational Physics 114 (2) (1994) 185–200. doi:10.1006/jcph.1994.1159.
URL http://www.sciencedirect.com/science/article/pii/S0021999184711594

[25] F. Treyssède, K. L. Nguyen, A. S. Bonnet-BenDhia, C. Hazard, Finite element computation of trapped and leaky elastic waves in open stratified waveguides, Wave Motion 51 (7) (2014) 1093–1107. doi:10.1016/j.wavemoti.2014.05.003.
URL http://www.sciencedirect.com/science/article/pii/S0165212514000742

[26] K. L. Nguyen, F. Treyssède, C. Hazard, Numerical modeling of three-dimensional open elastic waveguides combining semi-analytical finite element and perfectly matched layer methods, Journal of Sound and Vibration 344 (2015) 158–178. doi:10.1016/j.jsv.2014.12.032.
URL http://www.sciencedirect.com/science/article/pii/S0022460X14010360

[27] F. Treyssède, Spectral element computation of high-frequency leaky modes in three-dimensional solid waveguides, Journal of Computational Physics 314 (2016) 341–354. doi:10.1016/j.jcp.2016.03.029.
URL http://www.sciencedirect.com/science/article/pii/S0021999116001819

[28] W. Duan, R. Kirby, P. Mudge, T.-H. Gan, A one dimensional numerical approach for computing the eigenmodes of elastic waves in buried pipelines, Journal of Sound and Vibration 384 (2016) 177–193. doi:10.1016/j.jsv.2016.08.013.
URL http://www.sciencedirect.com/science/article/pii/S0022460X16304011

[29] H. Gravenkamp, C. Birk, C. Song, The computation of dispersion relations for axisymmetric waveguides using the Scaled Boundary Finite Element Method, Ultrasonics 54 (5) (2014) 1373–1385. doi:10.1016/j.ultras.2014.02.004.
URL https://www.sciencedirect.com/science/article/pii/S0041624X14000353

[30] H. Gravenkamp, C. Birk, C. Song, Computation of dispersion curves for embedded waveguides using a dashpot boundary condition, The Journal of the Acoustical Society of America 135 (3) (2014) 1127–1138. doi:10.1121/1.4864303.
URL http://scitation.aip.org/content/asa/journal/jasa/135/3/10.1121/1.4864303

[31] H. Gravenkamp, C. Birk, C. Song, Numerical modeling of elastic waveguides coupled to infinite fluid media using exact boundary conditions, Computers & Structures 141 (2014) 36–45. doi:10.1016/j.compstruc.2014.05.010.
URL http://www.sciencedirect.com/science/article/pii/S0045794914001242

[32] H. Gravenkamp, C. Birk, J. Van, Modeling ultrasonic waves in elastic waveguides of arbitrary cross-section embedded in infinite solid medium, Computers & Structures 149 (2015) 61–71. doi:10.1016/j.compstruc.2014.11.007.
URL http://www.sciencedirect.com/science/article/pii/S0045794914002788

[33] K.-J. Bathe, Finite Element Procedures, 2nd Edition, Klaus-Jurgen Bathe, Watertown, MA, 2006.

[34] V. Damljanović, R. L. Weaver, Forced response of a cylindrical waveguide with simulation of the wavenumber extraction problem, The Journal of the Acoustical Society of America 115 (4) (2004) 1582. doi:10.1121/1.1675818.
URL http://link.aip.org/link/JASMAN/v115/i4/p1582/s1&Agg=doi

[35] A. D. Pierce, Acoustics: An Introduction to Its Physical Principles and Applications, reprint Edition, Acoustical Society of America, 1989.

[36] C. M. Nilsson, S. Finnveden, Waves in thin-walled fluid-filled ducts with arbitrary cross-sections, Journal of Sound and Vibration 310 (1-2) (2008) 58–76. doi:10.1016/j.jsv.2007.07.081.
URL http://www.sciencedirect.com/science/article/pii/S0022460X0700644X

[37] P. Kudela, M. Krawczuk, W. Ostachowicz, Wave propagation modelling in 1d structures using spectral finite elements, Journal of Sound and Vibration

300 (1-2) (2007) 88–100. doi:10.1016/j.jsv.2006.07.031.
URL http://www.sciencedirect.com/science/article/pii/S0022460X0600647X

[38] W. Ostachowicz, P. Kudela, M. Krawczuk, A. Żak, Guided Waves in Structures for SHM: The Time-Domain Spectral Element Method, John Wiley & Sons, Ltd, Chichester, 2012.

[39] G. Karniadakis, S. J. Sherwin, Spectral/hp Element Methods for CFD, Oxford University Press, New York, Oxford, 1999.

[40] M. I. Gerritsma, T. N. Phillips, Spectral Element Methods for Axisymmetric Stokes Problems, Journal of Computational Physics 164 (1) (2000) 81–103. doi:10.1006/jcph.2000.6574.
URL http://www.sciencedirect.com/science/article/pii/S0021999100965744

[41] A. Fournier, Incompressible Fluid Flows in Rapidly Rotating Cavities, PhD thesis, 2004.

[42] T. Nissen-Meyer, A. Fournier, F. A. Dahlen, A two-dimensional spectral-element method for computing spherical-earth seismograms - I. Moment-tensor source, Geophysical Journal International 168 (3) (2007) 1067–1092. doi:10.1111/j.1365-246X.2006.03121.x.
URL http://gji.oxfordjournals.org/content/168/3/1067

[43] A. Bottero, P. Cristini, D. Komatitsch, M. Asch, An axisymmetric time-domain spectral-element method for full-wave simulations: Application to ocean acoustics, The Journal of the Acoustical Society of America 140 (5) (2016) 3520–3530. doi:10.1121/1.4965964.
URL http://asa.scitation.org/doi/10.1121/1.4965964

[44] F. Treyssède, L. Laguerre, Numerical and analytical calculation of modal excitability for elastic wave generation in lossy waveguides, The Journal of the Acoustical Society of America 133 (6) (2013) 3827–3837.

doi:10.1121/1.4802651.
URL http://scitation.aip.org/content/asa/journal/jasa/133/6/10.1121/1.4802651

[45] C. Aristégui, M. J. S. Lowe, P. Cawley, Guided waves in fluid-filled pipes surrounded by different fluids, Ultrasonics 39 (5) (2001) 367–375. doi:10.1016/S0041-624X(01)00064-6.
URL http://www.sciencedirect.com/science/article/pii/S0041624X01000646

[46] A. C. D. Royal, P. R. Atkins, M. J. Brennan, D. N. Chapman, H. Chen, A. G. Cohn, K. Y. Foo, K. F. Goddard, R. Hayes, T. Hao, P. L. Lewin, N. Metje, J. M. Muggleton, A. Naji, G. Orlando, S. R. Pennock, M. A. Redfern, A. J. Saul, S. G. Swingler, P. Wang, C. D. F. Rogers, Site Assessment of Multiple-Sensor Approaches for Buried Utility Detection, International Journal of Geophysics 2011 (2011) e496123. doi:10.1155/2011/496123.
URL https://www.hindawi.com/journals/ijge/2011/496123/abs/

[47] J. M. Muggleton, E. Rustighi, 'Mapping the Underworld': recent developments in vibro-acoustic techniques to locate buried infrastructure, Géotechnique Letters 3 (3) (2013) 137–141. doi:10.1680/geolett.13.00032.
URL http://www.icevirtuallibrary.com/doi/10.1680/geolett.13.00032